Defects and persistent luminescence in Eu-doped SrAl₂O₄

Khang Hoang*

Center for Computationally Assisted Science and Technology & Department of Physics, North Dakota State University, Fargo, North Dakota 58108, United States (Dated: November 9, 2022)

We investigate native point defects and rare-earth (co)dopants in $SrAl_2O_4$ using hybrid density-functional defect calculations. Europium (Eu) and dysprosium (Dy) are found to be mixed valence and energetically most favorable at the Sr lattice sites. However, unlike Eu where both Eu^{2+} and Eu^{3+} can be realized in synthesis, Dy is stable predominantly as Dy^{3+} , and the divalent Dy^{2+} may only be photogenerated under irradiation. On the basis of an analysis of Eu-related band-defect (including charge-transfer) and interconfigurational 5d-4f optical transitions, we assign the characteristic broad blue (445 nm) and green (520 nm) emission bands in Eu^{2+} -doped $SrAl_2O_4$ to the $4f^65d^1 \rightarrow 4f^7$ transition in Eu^{2+} incorporated at the Sr1 and Sr2 sites, respectively. Strontium interstitials (not oxygen vacancies, in contrast to what is commonly believed) and Dy_{Sr} can act as efficient electron traps for room-temperature persistent luminescence. This work calls for a reassessment of certain assumptions regarding specific carrier trapping centers made in all mechanisms previously proposed for the persistent luminescence in Eu- and (Eu,Dy)-doped $SrAl_2O_4$. It also serves as a methodological template for the understanding and design of rare-earth doped phosphors.

I. INTRODUCTION

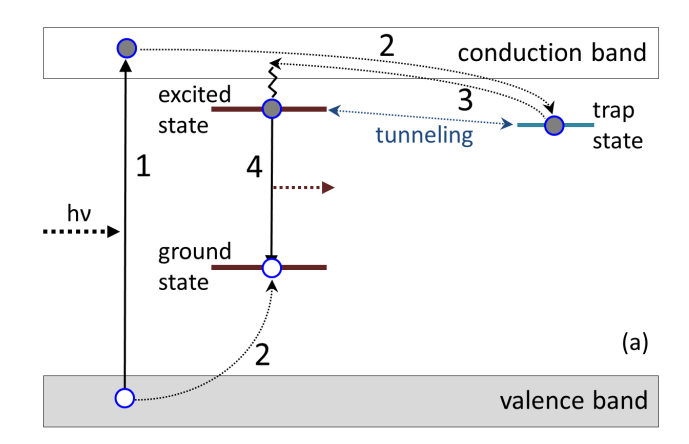
Persistent luminescence, previously often referred to as phosphorescence or long-lasting phosphorescence, is an intriguing phenomenon in which a material re-emits light over long periods of time after the excitation has stopped [1, 2]. Persistent luminescent materials (or persistent phosphors) have numerous applications and potential applications in safety signage and toys, road markings, solid-state lighting (flicker reduction), bio-imaging, nighttime solar energy, and photocatalysis [3]. Scientific research on persistent luminescence really took off since the discovery of (Eu,Dy)-doped SrAl₂O₄ by Murayam, Takeuchi, Aoki, and Matsuzawa of Nemoto & Co., Ltd. (Japan) in 1993; the material was found to produce extremely bright green and long-lasting (over many hours) luminescence in the dark [4, 5]. Three decades after the seminal work of the Nemoto researchers, although there has been great progress in understanding the phenomenon and in discovering new persistent phosphors—as it has already been documented in many excellent review articles and book chapters published in the last several years [1–3, 6–8], details of the underlying mechanism for the persistent luminescence observed in rare-earth (RE) doped SrAl₂O₄ and similar materials are still under debate, and the search for new or improved persistent phosphors, in general, remains largely trial and error.

The optical properties of Eu-doped $SrAl_2O_4$ are characterized by a broad green emission band peaking at 520 nm at room temperature [9–11]. At lower temperatures, another peak occurs in the emission spectrum at 450 nm (blue) [12]. In addition, a broader excitation band peaking at 276 nm or 250 nm and sharp Eu^{3+} 4f–4f transitions in the excitation and emission spectra have also been reported [13–15]. Co-doping the material with Dy

does not change the emission spectrum, but strongly enhances the afterglow time and intensity [5]. There are currently about a dozen different mechanisms proposed in the literature to explain the persistent luminescence observed in Eu- and (Eu,Dy)-doped SrAl₂O₄ [5, 16–23]. All these mechanisms involve defect levels induced by the RE (co)dopants and/or native point defects. Oxygen vacancies, in particular, have been invoked in many mechanisms as electron trapping centers responsible for the delayed emission. Figure 1 shows a currently generally accepted mechanism involving electron trapping and detrapping processes (a mechanism involving hole trapping and detrapping is similar) [2]. In the context of Eu²⁺-doped SrAl₂O₄, the emission center is expected to be Eu²⁺ with the ground and excited states being $4f^7$ and $4f^65d^1$, respectively, and the trapping center can be native defects and/or RE co-dopants or other impurities.

Due to the lack of a detailed understanding of defect physics in SrAl₂O₄, all the proposed mechanisms [5, 16–23] are highly speculative about specific emission centers and charge carrier trapping centers. This has been a major obstacle toward rational design of persistent phosphors with improved performance. Here, we present an investigation of native defects and RE (co)dopants in monoclinic SrAl₂O₄ using first-principles defect calculations. The hybrid density-functional theory (DFT)/Hartree-Fock method [24] employed here has been shown to be successful in the study of defects in semiconductors and insulators in general [25] and REdoped materials in particular [26–28]. On the basis of our results, we identify dominant native defects, discuss the stable valence states of the RE (co)dopants, and determine all energy levels induced by the defects. Eu-related optical transitions, including band-defect and interconfigurational Eu²⁺ 5d-4f absorption and emission processes, are investigated to identify sources of the broad absorption and emission bands observed in experiments, including the characteristic blue and green emissions.

^{*} khang.hoang@ndsu.edu



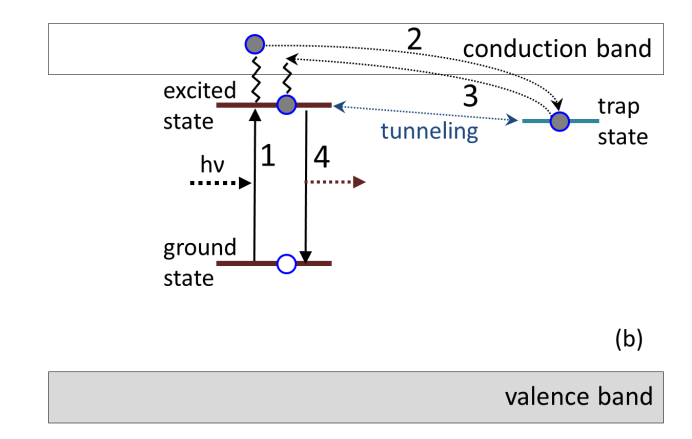


FIG. 1. Schematic illustration of a persistent luminescence mechanism under (a) band-to-band or (b) below-gap excitation: (1) excitation: electrons are excited and holes generated under illumination; (2) trapping: the excited electrons (generated holes) are captured nonradiatively by electron (hole) traps through the conduction (valence) band and/or via quantum tunneling; (3) detrapping: the trapped electrons are released under thermal stimulation; (4) recombination: the released electrons return to the emission center and recombine with holes, resulting in a delayed luminescence. Adapted from Xu and Tanabe [2]

II. METHODOLOGY

We model defects (i.e., native point defects and impurities) in $SrAl_2O_4$ using a supercell approach in which a defect is included in a periodically repeated finite volume of the host material. The formation energy of a defect X in effective charge state q (with respect to the host lattice) is defined as [25, 29]

$$E^{f}(\mathbf{X}^{q}) = E_{\text{tot}}(\mathbf{X}^{q}) - E_{\text{tot}}(\text{bulk}) - \sum_{i} n_{i} \mu_{i}$$
 (1)
+ $q(E_{\text{v}} + \mu_{e}) + \Delta^{q}$,

where $E_{\rm tot}({\bf X}^q)$ and $E_{\rm tot}({\rm bulk})$ are the total energies of the defect-containing and perfect bulk supercells, respectively; n_i is the number of atoms of species i that have been added $(n_i>0)$ or removed $(n_i<0)$ to form the defect; μ_i is the atomic chemical potential, representing the energy of the reservoir with which atoms are being exchanged, and referenced to the total energy per atom of i in its elemental phase at 0 K. μ_e is the chemical potential of electrons, i.e., the Fermi level, representing the energy of the electron reservoir, referenced to the valence-band maximum (VBM) in the bulk $(E_{\rm v})$. Finally, Δ^q is the correction term to align the electrostatic potentials of the bulk and defect supercells and to account for finite-size effects on the total energies of charged defects [30, 31].

Under thermodynamic equilibrium, the concentration of a defect is directly related to its formation energy [29]:

$$c = N_{\text{sites}} N_{\text{config}} \exp\left(\frac{-E^f}{k_{\text{B}}T}\right),$$
 (2)

where $N_{\rm sites}$ is the number of high-symmetry sites in the lattice (per unit volume) on which the defect can be incorporated, $N_{\rm config}$ is the number of equivalent configurations (per site), and $k_{\rm B}$ is the Boltzmann constant. At

a given temperature, a defect with a lower formation energy occurs with a higher concentration. Note, however, that when a material is prepared under non-equilibrium conditions excess defects can be frozen-in and the equilibrium concentration is only the lower bound.

While the Fermi level in Eq. (1) can be treated as a variable, it is not a free parameter. The actual Fermi-level position of the material can be determined by solving the charge-neutrality equation [29]:

$$\sum_{i} c_i q_i - n_e + n_h = 0, (3)$$

where c_i and q_i are the concentration and charge, respectively, of defect X_i ; n_e and n_h are free electron and hole concentrations, respectively; and the summation is over all possible defects present in the material.

The thermodynamic transition level between charge states q and q' of a defect, $\epsilon(q/q')$, is defined as the Fermilevel position at which the formation energy of the defect in charge state q is equal to that in state q' [25], i.e.,

$$\epsilon(q/q') = \frac{E^f(X^q; \mu_e = 0) - E^f(X^{q'}; \mu_e = 0)}{q' - q}, \quad (4)$$

where $E^f(X^q; \mu_e = 0)$ is the formation energy of the defect X in charge state q when the Fermi level is at the VBM ($\mu_e = 0$). This $\epsilon(q/q')$ level [also referred to as the (q/q') level], corresponding to a defect energy level (or, simply, defect level), would be observed in experiments where the defect in the final charge state q' fully relaxes to its equilibrium configuration after the transition.

Defect-to-band and band-to-defect optical transitions, including those of the charge-transfer type [32], can be characterized using the *optical* transition level $E_{\rm opt}^{q/q'}$ that is defined similarly to $\epsilon(q/q')$ but with the total energy

of the final state q' calculated using the lattice configuration of the initial state q [25]. For the 5d–4f transitions in neutral Eu defects, we calculate the energies based on a constrained occupancy approach and Δ SCF analysis (SCF: self-consistent field), similar to that used in previous studies of RE-doped phosphors [33, 34]. In this approach, we create the excited state Eu $4f^65d^1$ in $\mathrm{SrAl_2O_4}$ by manually emptying the highest Eu 4f state and filling the next state lying higher in energy.

The total-energy electronic structure calculations are based on DFT with the Heyd-Scuseria-Ernzerhof (HSE) functional [24], the projector augmented wave (PAW) method [35], and a plane-wave basis set, as implemented in the Vienna Ab Initio Simulation Package (VASP) [36]. Along with the CPU version, the GPU port of VASP (version 6.2.1) is also used. The Hartree-Fock mixing parameter is set to 0.33 and the screening length to the default value of 10 Å to match the experimental band gap. We use the PAW potentials in the VASP database which treat Sr $4s^24p^65s^2$, Al $3s^23p^1$, O $2s^22p^4$, Eu $5s^25p^64f^76s^2$, and Dy $5s^25p^64f^{10}6s^2$ explicitly as valence electrons and the rest as core. Defects are modelled using monoclinic $2\times1\times3$ (168-atom) supercells and integrations over the Brillouin zone are performed using the Γ point, except in the constrained occupancy calculations (using VASP 5.3.3) where $1\times1\times3$ (84-atom) supercells and a Γ -centered $2\times2\times1$ k-point mesh are used. In the defect calculations, the lattice parameters are fixed to the calculated bulk values but all the internal coordinates are relaxed. In all the calculations, the plane-wave basis-set cutoff is set to 500 eV and spin polarization is included: structural relaxations are performed with the HSE functional and the force threshold is chosen to be 0.02 eV/Å. Spin-orbit interaction is not included as it has negligible effects on the defect transition levels [28].

The chemical potentials of Sr, Al, and O vary over a range determined by requiring that the host compound $SrAl_2O_4$ is stable against competing Sr-Al-O phases; see Sec. III A. Experimentally relevant or representative sets of μ_{Sr} , μ_{Al} , and μ_{O} are adopted to present defect formation energies. The chemical potential of Dy is obtained by assuming equilibrium with Dy_2O_3 ; that of Eu by assuming equilibrium with Eu_2O_3 (under oxidizing conditions) or EuO (under reducing conditions). It should be noted that the transition levels $\epsilon(q/q')$ and $E_{opt}^{q/q'}$ are independent of the choice of the atomic chemical potentials.

III. RESULTS AND DISCUSSION

A. Bulk properties

 $SrAl_2O_4$ crystallizes in the monoclinic $P2_1$ space group [37]; see Fig. 9 in Appendix A. Its crystal structure has two inequivalent Sr lattice sites, four inequivalent Al sites, and eight inequivalent O sites. The Sr sites, Sr1 and Sr2, are in channels along the c-axis formed by the Al–O framework (hereafter referred to as the Sr1 and Sr2 chan-

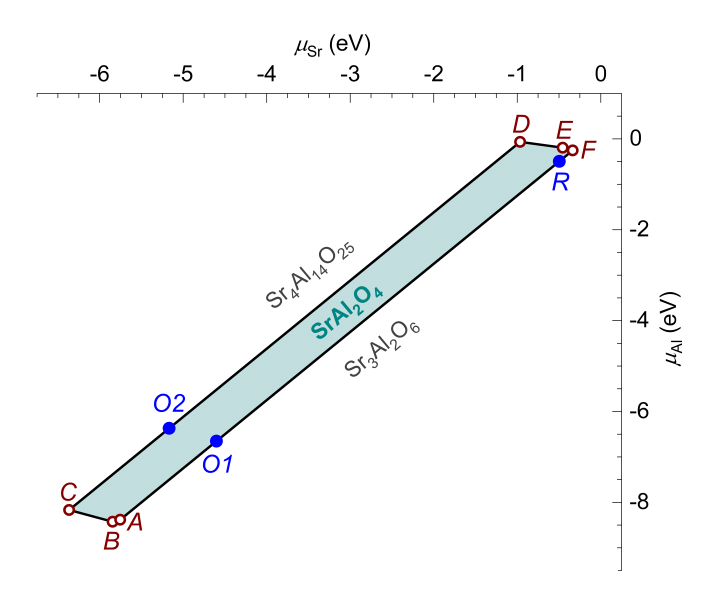


FIG. 2. Chemical-potential phase diagram for $SrAl_2O_4$. Sr-Al-O phases that define the stability region of the host, shown as a shaded polygon, are SrO_2 (the AB line), O_2 (BC), $Sr_4Al_1_4O_2_5$ (CD), $SrAl_4$ (DE), $SrAl_2$ (EF), and $Sr_3Al_2O_6$ (FA). Points O1, O2, and R are examples of experimentally relevant oxidizing and reducing environments; see the text.

nels). The calculated lattice parameters are a = 8.4491Å, b = 8.8159 Å, c = 5.1525 Å, and $\beta = 93.5397^{\circ}$, in excellent agreement with the experimental values [37]. The calculated band gap is 6.51 eV, an indirect gap with the valence-band maximum (VBM) at the X point in the Brillouin zone and the conduction-band minimum (CBM) at the Γ point. For comparison, the reported experimental band gap is 6.5-6.6 eV [5, 38, 39]. The VBM consists primarily of the O 2p states, whereas the CBM consists of a mixture of the Sr, Al, and O s states. The total static dielectric constant is calculated to be 9.36 (taken as the average of the xx, yy, and zz components) with the electronic contribution based on the real part of the dielectric function $\epsilon_1(\omega)$ for $\omega \to 0$ obtained within HSE and the ionic contribution calculated using density-functional perturbation theory [40] within the generalized-gradient approximation [41].

Figure 2 shows the phase stability of $SrAl_2O_4$. The formation enthalpies (calculated at 0 K) of different Sr-Al-O phases are listed in Table I in Appendix A. The initial structures of these phases are taken from the Materials Project database [42]. The stability region of $SrAl_2O_4$ is delineated mainly by $Sr_3Al_2O_6$ and $Sr_4Al_{14}O_{25}$, which is consistent with the experimental phase diagram [43, 44].

In the presentation of defect formation energies in the next sections, we make use of the following points in the phase diagram: (i) O1, where the host compound is in equilibrium with $\rm Sr_3Al_2O_6$ and air (the oxygen partial pressure $p_{\rm O_2}=0.21$ atm) at $750^{\circ}\rm C$, (ii) O2, where the host is in equilibrium with $\rm Sr_4Al_{14}O_{25}$ and air at $750^{\circ}\rm C$, and (iii) R, where the host is in equilibrium with

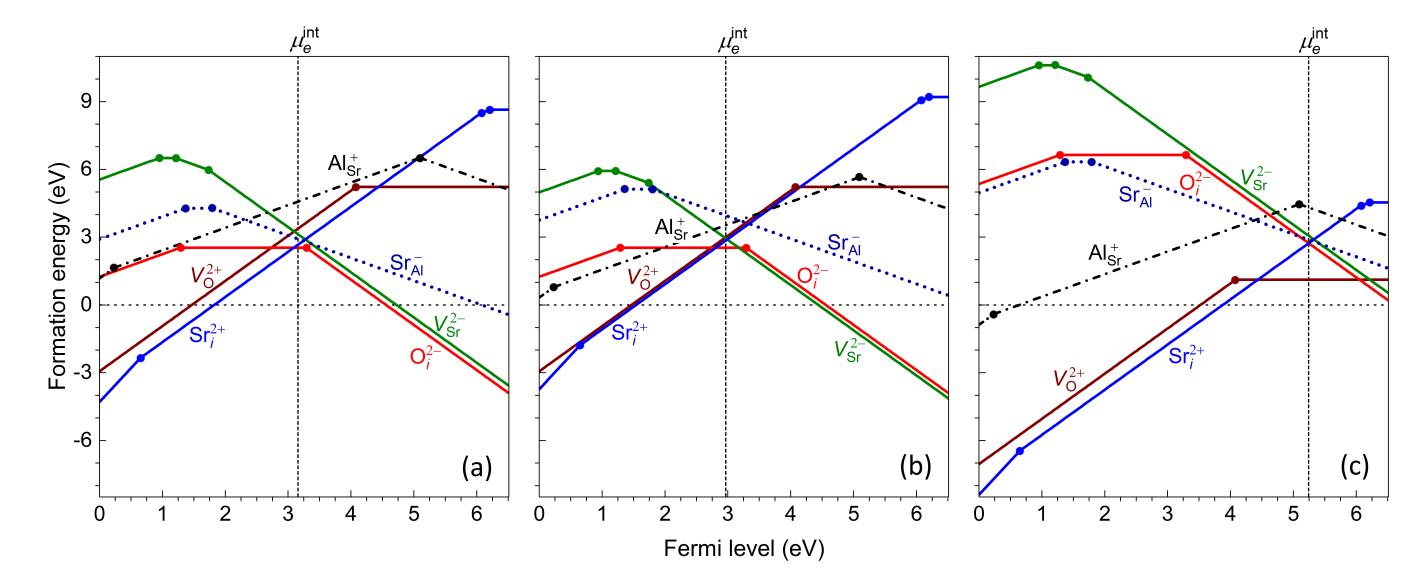


FIG. 3. Formation energies of native defects in $SrAl_2O_4$, as a function of the Fermi level from the VBM (0 eV) to the CBM (6.51 eV), calculated at points (a) O1, (b) O2, and (c) R in the phase diagram (Fig. 2). For each defect, only segments of the formation energy lines corresponding to the lowest-energy charge states are shown. The slope of these segments indicates the charge state q: positively (negatively) charged defect configurations have positive (negative) slopes; horizontal segments correspond to neutral defect configurations. Large dots connecting two segments with different slopes mark the defect levels $\epsilon(q/q')$. For a defect with multiple inequivalent lattice sites, only the lowest-energy lattice site is reported.

 ${\rm Sr_3Al_2O_6}$ and ${\rm Ar/H_2}$ 5% ($p_{\rm O_2}\sim 10^{-20}$ atm) at 1400°C. Points O1 and O2 (with $\mu_{\rm O}=-1.20$ eV) represent oxidizing environments, whereas point R ($\mu_{\rm O}=-5.30$ eV) represents a highly reducing environment. Here, $\mu_{\rm O}$ is calculated as half of the Gibbs free energy of ${\rm O_2}$ gas at the given T and $p_{\rm O_2}$ values [45]. These conditions are chosen to reflect the conditions under which undoped and Eudoped ${\rm SrAl_2O_4}$ samples are often prepared. Beauger [16] reported the presence of ${\rm Sr_3Al_2O_6}$ as an impurity phase, indicating that their synthesis environment corresponds to a point very close to the FA line in Fig. 2.

B. Native point defects

Figure 3 shows the formation energy of native defects in $SrAl_2O_4$. The defects introduce one or more energy levels in the host's band gap region (marked by large dots in the figure; explicit numerical values are listed in Table II). Under the experimentally relevant conditions (see Sec. III A), the dominant defects (i.e., those with the lowest formation energy) are Sr and O vacancies and interstitials. In the absence of impurities, intentionally doped or unintentionally present, the Fermi level is "pinned" at the position $\mu_e^{\rm int}$ ("int" for intrinsic), determined predominantly by the lowest-energy charged defects, where the charge neutrality condition (3) is maintained. From one point in the phase diagram (Fig. 2) to another, the defect landscape in $SrAl_2O_4$ changes, leading to a change in the $\mu_e^{\rm int}$ value; e.g., $\mu_e^{\rm int}$ moves toward the CBM in going from oxidizing (points O1 and O2) to reducing (point R)

synthesis conditions. We find that $\mu_e^{\rm int}$ varies from 2.28 eV (under the conditions at point C) to 5.36 eV (point F). The Fermi level of ${\rm SrAl_2O_4}$, even in the presence of intentional and/or unintentional impurities, cannot be close to the VBM (under all synthesis conditions) but can, in principle, be high up at the CBM (under reducing synthesis conditions only). This is because the formation energy of certain native defects, specifically Sr interstitials and O vacancies, is negative in the region near the VBM (up to $E_{\rm v}+0.94$ eV at point C and higher at other points in the phase diagram), whereas the native defects can all have a positive formation energy under the reducing conditions (e.g., those at points D-F and R).

The removal of an ${\rm O}^{2-}$ results in a positively charged O vacancy $(V_{\rm O}^{2+},\,{\rm spin}\,\,S=0)$. Other charge states, $V_{\rm O}^+$ (S=1/2) and $V_{\rm O}^0$ $(S=0),\,{\rm are}$ also stable. The energetics and electronic behavior of $V_{\rm O}$ are different at the inequivalent O lattice sites due to the slightly different local lattice environments. At certain O sites (e.g., at the O8 site as shown in Fig. 3), $V_{\rm O}^+$ is energetically less favorable than $V_{\rm O}^{2+}$ and $V_{\rm O}^0$ in the entire range of the Fermilevel values. Notably, the energy levels introduced by the vacancy at the O1 to O8 sites are all about 2.43–3.55 eV below the CBM; see Fig. 10. The lowest-energy $V_{\rm O}^{2+}$ configuration occurs at the O8 site, see Fig. 4(a), indicating that the Al–O8 bonds are weakest. The highest-energy $V_{\rm O}^{2+}$ occurs at the O1 site. Under reducing conditions (e.g., at point R), $V_{\rm O}$ occurs in the form of $V_{\rm O}^0$ with a high concentration (highest among all native defects).

Our results for the oxygen vacancies are thus in *sharp* contrast to those of Finley et al. [47] where the defect

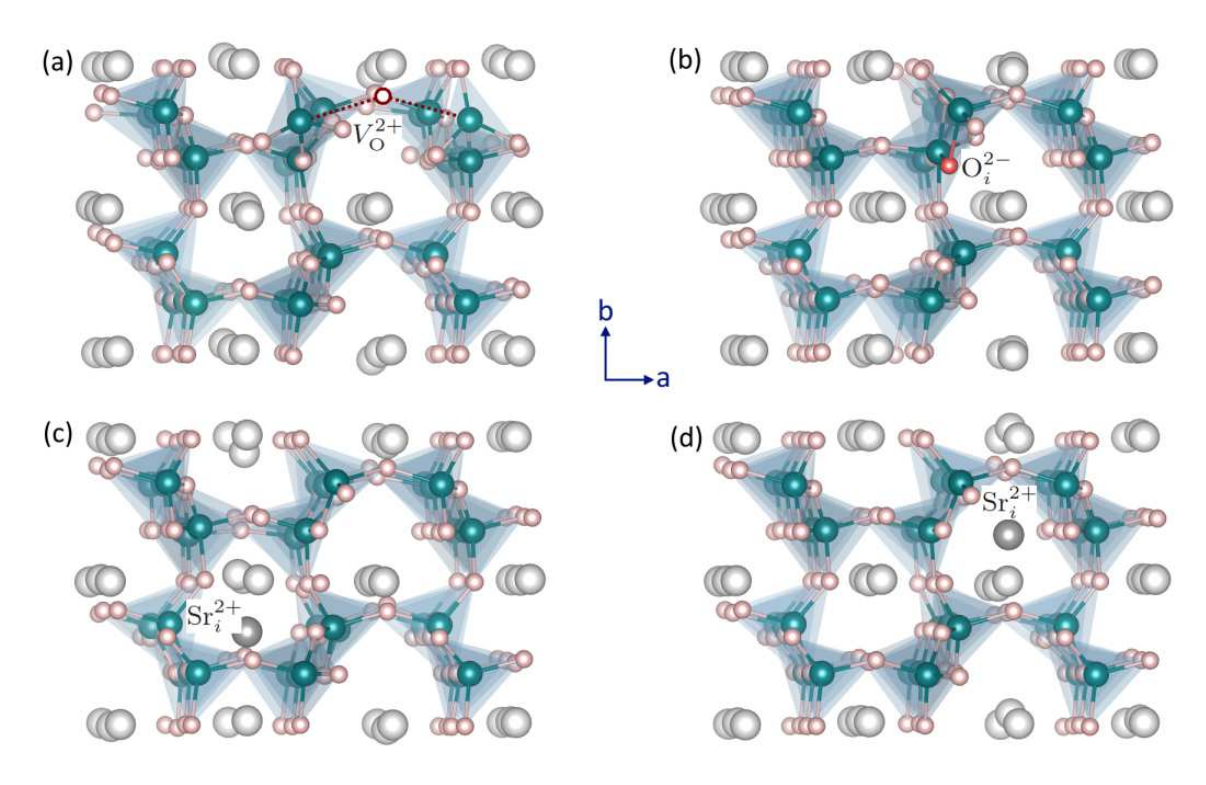


FIG. 4. Structures of selected native defect configurations in $SrAl_2O_4$: (a) V_O^{2+} at the O8 lattice site, (b) O_i^{2-} , (c) Sr_i^{2+} in the Sr1 channel, and (d) Sr_i^{2+} in the Sr2 channel. Large (gray) spheres are Sr, medium (blue) are Al, and small (red) are O. All the atomic structures in this work are visualized using the VESTA package [46].

energy levels introduced by $V_{\rm O}$ were found to scatter all over the upper half of the host band gap region. Given the similarity in the bonding environments of the inequivalent O sites (e.g., every single O atom is bonded to two Al atoms), the almost random distribution of the defect levels reported in Ref. [47] cannot be justified.

The addition of an oxygen, which results in an oxygen interstitial (O_i) , introduces energy levels near the midgap region; see also Table II. In the O_i^{2-} (S=0) configuration, the added O^{2-} is shared between two AlO₄ units; Fig. 4(b) [and Fig. 11(a)]. O_i^- (S=1/2; not visible in Fig. 3 due to its very small stability range) is a complex of O_i^{2-} and an electron hole localized at an O site (hereafter referred to as η_O^+ , S=1/2). The structure of O_i^0 [S=0; Fig. 11(b)] can be described as having the interstitial oxygen bonded to one of the O atoms in an AlO₄ unit (the O–O distance is 1.48 Å), resulting in a distorted AlO₅. O_i^+ (S=1/2) is a complex of O_i^0 and η_O^+ .

The removal of a Sr^{2+} ion from the host lattice results in a negatively charged Sr vacancy $(V_{\mathrm{Sr}}^{2-}, S=0)$. Other stable charge states of V_{Sr} are V_{Sr}^{-} $(S=1/2), V_{\mathrm{Sr}}^{0}$ (S=1), and V_{Sr}^{+} (S=3/2), which can be regarded as complexes consisting of V_{Sr}^{2-} and one, two, and three η_{O}^{+} defects, respectively. V_{Sr} at the $\mathrm{Sr}1$ site is slightly lower in energy than that at the $\mathrm{Sr}2$ site, e.g., by 0.08 eV in the case of V_{Sr}^{2-} . The defect levels associated with V_{Sr} are in the lower half of the band gap region; see also Table II.

There are two possible sites for Sr interstitials (Sr_i) :

one, Sr_{i1} , locating in the Sr1 channel (along the c-axis) but off the Sr1 chain and between two Al atoms (along the a-axis), see Fig. 4(c), and the other, Sr_{i2} , in the Sr2 channel but off the Sr2 chain and between two Al atoms (along the a-axis), see Fig. 4(d) [and Fig. 11(c)]. Sr_{i1} and Sr_{i2} are approximately at the interstitial sites V2 and V1, respectively, mentioned in Bierwagen et al. [14]. Sr_{i2} is lower in energy than Sr_{i1} (e.g., by 0.19 eV in the case of Sr_{i}^{2+} , S=0). The defect introduces three defect levels: one above the VBM and two just below the CBM. The other charge states are Sr_{i}^{3+} (S=1/2; a complex of Sr_{i}^{2+} and η_{O}^{+}), Sr_{i}^{+} (S=1/2), and Sr_{i}^{0} (S=0). At μ_{e}^{int} , Sr_{i}^{2+} is energetically most stable among the stable charge states of Sr_{i} and one of the lowest-energy native defects.

Antisite defects, Al_{Sr} and Sr_{Al} , are also considered. We find that they are higher in energy than the Sr and O vacancies and interstitials. Al_{Sr} is lower in energy at the Sr2 site than at the Sr1 site, e.g., 0.55 eV lower in the case of Al_{Sr}^+ (S=0); Al_{Sr}^{2+} (S=1/2) is a complex of Al_{Sr}^+ and η_O^+ . Sr_{Al} is energetically most favorable at the Al2 site; Sr_{Al}^0 (S=1/2) and Sr_{Al}^+ (S=1) are defect complexes of Sr_{Al}^- and one and two η_O^+ , respectively. Finally, the creation of Al vacancies (V_{Al}) involves breaking four strongly covalent Al–O bonds, a high energy process. Such defects, as well as Al interstitials (Al_i), have high formation energies and are thus not included here.

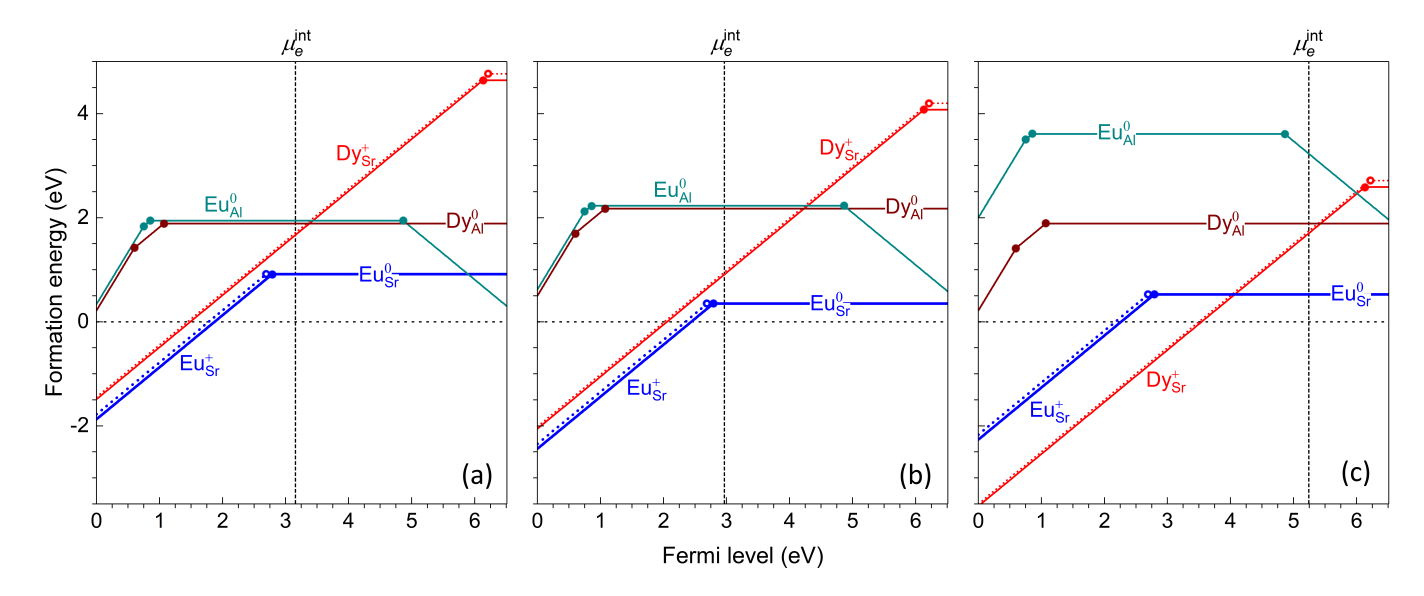


FIG. 5. Formation energies of Eu- and Dy-related defects in SrAl₂O₄, calculated at points (a) O1, (b) O2, and (c) R in the phase diagram (Fig. 2). Large dots connecting two segments with different slopes mark the *defect levels*. For Eu_{Sr} and Dy_{Sr}, the defect configurations at both the Sr1 (dotted lines) and Sr2 (solid lines) sites are included.

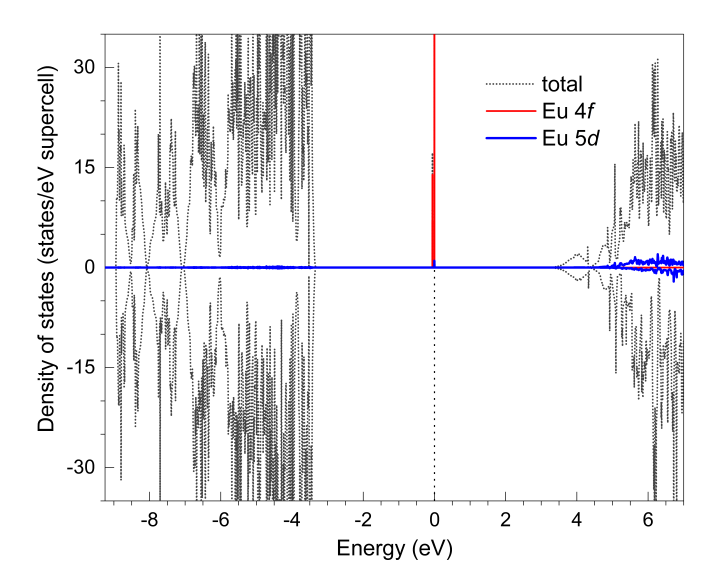


FIG. 6. Total and projected densities of states of Eu-doped ${\rm SrAl_2O_4}$, specifically the ${\rm Eu_{Sr}^0}$ defect configuration with the chemical composition ${\rm Eu}_x{\rm Sr}_{1-x}{\rm Al}_2{\rm O}_4$ (x=0.125). The zero of energy is set to the highest occupied state.

C. Rare-earth (co)dopants

Figure 5 shows the formation energy of substitutional Eu and Dy impurities at the Sr and Al sites. Results for the REs at the interstitial sites are included in Fig. 12. Table II lists explicit numerical values of the energy levels and stable RE ions. We find that, at and near the Fermi level determined by the native defects ($\mu_e^{\rm int}$), RE_{Sr} is lower in energy than RE_{Al} and RE_i, indicating that Eu and Dy are incorporated into SrAl₂O₄ at the Sr sites.

 $\rm Eu_{Sr}$ is stable as $\rm Eu_{Sr}^0$ (i.e., $\rm Eu^{2+},$ with a magnetic moment of $7\mu_{\rm B};$ spin S=7/2) and/or $\rm Eu_{Sr}^+$ (i.e., Eu^{3+}, with a magnetic moment of $6\mu_{\rm B};~S=3)$. The Eu $_{\rm Sr}^0$ configurations at the Sr1 and Sr2 sites are almost degenerate in energy, whereas $\mathrm{Eu}_{\mathrm{Sr}}^+$ at the Sr2 site is 0.09 eV lower in energy than at the Sr1 site. The (+/0) level of Eu_{Sr} is 2.69 eV above the VBM when incorporated at the Sr1 site or 2.79 eV when incorporated at the Sr2 site; below (above) this level, $\mathrm{Eu^{3+}}$ ($\mathrm{Eu^{2+}}$) is energetically more favorable. The $\mathrm{Eu^{2+}}/\mathrm{Eu^{3+}}$ ratio thus depends on the actual position of the Fermi level which, in turn, depends on the synthesis conditions. The ratio is high under reducing conditions (e.g., at point R) and decreases as one changes from reducing to oxidizing conditions. Note that, under actual synthesis conditions and as Eu-doped SrAl₂O₄ is typically prepared using Eu³⁺ as dopant, an equilibrium assumption may not hold true, and the trivalent ion may be frozen in [14]. In other words, Eu³⁺ may be present even in samples prepared under less oxidizing conditions.

The mixed valence of Eu in $\mathrm{SrAl_2O_4}$ can be understood based on the calculated electronic structure of $\mathrm{Eu_{Sr}^0}$, reported in Fig. 6. The HSE calculations of the electronic density of states are carried out using a smaller, $1\times1\times2$ supercell and a Γ -centered $3\times3\times3$ k-point mesh. $\mathrm{Eu_{Sr}^0}$ has seven occupied spin-up 4f states in the host band gap (and seven spin-down unoccupied 4f states deep in the conduction band). Given the electronic structure, when one electron is removed from this neutral defect configuration, the electron is removed from the highest occupied state (which is the highest $\mathrm{Eu}\ 4f$ state). This results in the divalent $\mathrm{Eu^{2+}}\ (4f^7)$ being oxidized to the trivalent $\mathrm{Eu^{3+}}\ (4f^6)$, i.e., $\mathrm{Eu_{Sr}^0}$ to $\mathrm{Eu_{Sr}^+}$. Figure 13(a) shows the localized $\mathrm{Eu}\ 4f$ electron associated with $\mathrm{Eu_{Sr}^0}$.

At and near μ_e^{int} , Eu_{Al} is stable as Eu_{Al} (i.e., Eu³⁺)

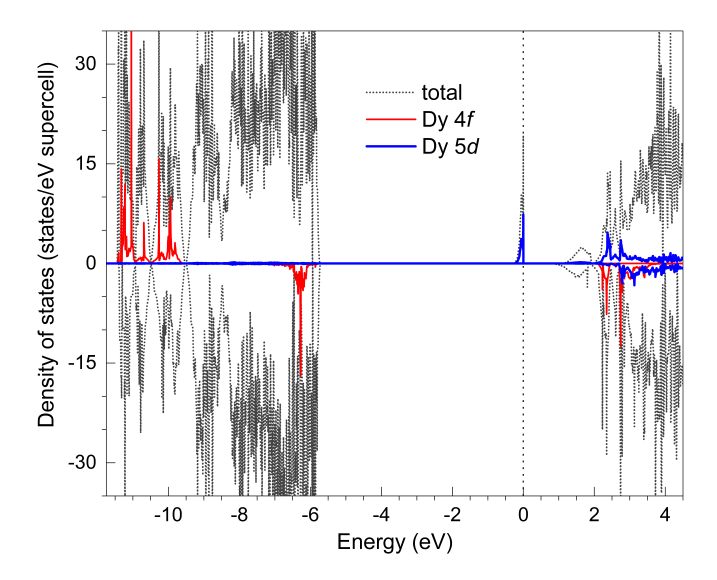


FIG. 7. Total and projected densities of states of Dy-doped $SrAl_2O_4$, specifically the Dy_{Sr}^0 defect configuration with the chemical composition $Dy_xSr_{1-x}Al_2O_4$ (x=0.125). The zero of energy is set to the highest occupied state.

under the oxidizing conditions (O1 and O2), and as $\operatorname{Eu}_{\operatorname{Al}}^-$ (i.e., Eu^{2+}) and/or $\operatorname{Eu}_{\operatorname{Al}}^0$ under the reducing condition (R). Other electronically stable charge states are $\operatorname{Eu}_{\operatorname{Al}}^+$ (a complex of $\operatorname{Eu}_{\operatorname{Al}}^0$ and $\operatorname{Eu}_{\operatorname{Al}}^{2+}$ (a complex of $\operatorname{Eu}_{\operatorname{Al}}^0$ and two $\eta_{\operatorname{O}}^+$). These positively charged states, however, cannot be obtained during synthesis due to the negative formation energies of $\operatorname{Eu}_{\operatorname{Sr}}$ and the native defects in the region above the VBM. We find that, at and near $\mu_e^{\operatorname{int}}$, Eu_i is electronically stable as Eu_i^{2+} (i.e., Eu^{2+}) and has a much higher formation energy than $\operatorname{Eu}_{\operatorname{Sr}}$ and $\operatorname{Eu}_{\operatorname{Al}}$.

The mixed valence of Eu is well discussed in the experimental literature [14, 16, 19, 48]. The fact that both $\mathrm{Eu^{3+}}$ and $\mathrm{Eu^{2+}}$ can be realized in as-prepared $\mathrm{SrAl_2O_4}$ is consistent with the above results showing the (+/0) level of $\mathrm{Eu_{Sr}}$ is located near midgap and the stability ranges of $\mathrm{Eu_{Sr}^+}$ and $\mathrm{Eu_{Sr}^0}$ are accessible during synthesis. Wang et al. [49] found $\mathrm{Eu^{2+}}$ to be distributed almost equally at the two Sr sites, consistent with the fact that the energies of $\mathrm{Eu_{Sr}^0}$ at the Sr1 and Sr2 sites are almost equal. Note that other valence states of Eu (e.g., $\mathrm{Eu^+}$, as proposed by Matsuzawa et al. [5]) cannot be stabilized electronically.

DySr is energetically favorable as DySr (i.e., Dy³+; S=5/2) in almost the entire range of the Fermi-level values and as DySr (i.e., Dy²+; S=3) in a small range below the CBM. The (+/0) level is located at 6.21 eV (6.13 eV) above the VBM, i.e., 0.30 eV (0.38 eV) from the CBM, at the Sr1 (Sr2) site. The defect is slightly lower in energy at the Sr2 site than at the Sr1 site; the difference is 0.12 eV for DySr or 0.05 eV for DySr. We find that the electronic configuration of Dy³+ is $4f^9$, whereas that of Dy²+ is $4f^9$ 5d¹. Figure 7 shows the electronic structure of DySr. The nine (seven spin-up and two spin-down) occupied Dy 4f states are in the valence band, the occupied Dy 5d¹ state is in the upper half of the host band gap, and

the five spin-down unoccupied Dy 4f states are in the conduction band. When one electron is removed from $\mathrm{Dy}_{\mathrm{Sr}}^0$, it is removed from the Dy $5d^1$ state, which leads to the formation of $\mathrm{Dy}_{\mathrm{Sr}}^+$. Figure 13(c) shows the localized Dy 5d electron associated with the $\mathrm{Dy}_{\mathrm{Sr}}^0$ configuration.

Dy $_{Al}$ is stable as Dy $_{Al}^{0}$ (i.e., Dy $^{3+}$), except near the VBM where it is stable as Dy $_{Al}^{+}$ (i.e., Dy $^{4+}$ with the electronic configuration $4f^{8}$) or Dy $_{Al}^{2+}$ (a complex of Dy $_{Al}^{+}$ and η_{O}^{+}). However, given the negative formation energy of Dysr and the native defects in the region above the VBM, these positive charge states are inaccessible during synthesis. Dy $_{i}$ is stable as Dy $_{i}^{3+}$; see Fig. 12. At and near μ_{e}^{int} , DyAl and Dy $_{i}$ are all higher energy than Dysr, indicating that Dy is incorporated at the Sr sites.

The results for the Dy-related defects thus confirm the stabilization of Dy_{Sr}, consistent with the fact that Dy is present as Dy³⁺ in as-prepared Dy-doped samples. Interestingly, Dy_{Sr}^0 (i.e., Dy^{2+}) is also found to be structurally and electronically stable. Dy_{Sr}^0 , however, has a very small stability range that is close to the CBM, and in that range $\rm Dy_{Sr}$ becomes much less favorable energetically than $\rm Dy_{Al}^0$ (i.e., $\rm Dy^{3+}),$ indicating that the divalent Dy²⁺ is almost impossible to obtain during synthesis. It can be photogenerated under irradiation nonetheless. Experimentally, Joos et al. [50] reported evidence of the Dv^{3+/2+} valence change in (Eu, Dy)-doped Sr₄Al₁₄O₂₅ under laser excitation. A similar process for Dy could be observed in SrAl₂O₄. Note that Dorenbos [20] estimated the "ground state of Dy^{2+} " to be at 0.9 eV below the CBM, based on a semiempirical model. Such a level is much lower than our calculated (+/0) level of Dy_{Sr}. Our results also show that Dy⁴⁺ is not stable electronically at the Sr site; the tetravalent ion is stable at the Al site but energetically unfavorable, as discussed above.

Finally, we consider possible association between Eu_{Sr} and Dy_{Sr} or a native defect. Figure 14 shows the formation energy of Eusr-Dysr, Eusr-Vo, Eusr-Oi, Eusr- $V_{\rm Sr}$, and Eu_{Sr}-Sr_i; see also Table III for details on the stable charge states of the complexes. Focusing on the Fermi-level range near the CBM, which is relevant to the physics under investigation, we find that the electronic behavior of the complexes is determined predominantly by the non-Eu constituent. Specifically, $(Eu_{Sr}-Dy_{Sr})^+$ is a defect complex consisting of $\operatorname{Eu_{Sr}^0}$ and $\operatorname{Dy_{Sr}^0}$ is a complex of $\operatorname{Eu_{Sr}^0}$ and $\operatorname{Dy_{Sr}^0}$; ($\operatorname{Eu_{Sr}^-}V_O$)⁰ is a complex of $\operatorname{Eu_{Sr}^0}$ and V_O^0 ; ($\operatorname{Eu_{Sr}^-}V_i$)² is a complex of $\operatorname{Eu_{Sr}^0}$ and $\operatorname{U_{Sr}^0}$; ($\operatorname{Eu_{Sr}^-}V_i$)² is a complex of $\operatorname{Eu_{Sr}^0}$ and $\operatorname{U_{Sr}^0}$; ($\operatorname{Eu_{Sr}^0}$)² is a complex of $\operatorname{Eu_{Sr}^0}$ and $\operatorname{U_{Sr}^0}$; ($\operatorname{Eu_{Sr}^0}$)² is a complex of $\operatorname{Eu_{Sr}^0}$ and $\operatorname{U_{Sr}^0}$; ($\operatorname{Eu_{Sr}^0}$)² is a complex of $\operatorname{Eu_{Sr}^0}$ and $\operatorname{U_{Sr}^0}$; ($\operatorname{Eu_{Sr}^0}$)² is a $\operatorname{Eu_{Sr}^0}$ and $\operatorname{U_{Sr}^0}$; ($\operatorname{Eu_{Sr}^0}$)² is a $\operatorname{Eu_{Sr}^0}$ and $\operatorname{U_{Sr}^0}$; ($\operatorname{Eu_{Sr}^0}$)² is a $\operatorname{U_{Sr}^0}$; ($\operatorname{Eu_{Sr}^0}$)² is a $\operatorname{Eu_{Sr}^0}$ and $\operatorname{U_{Sr}^0}$; ($\operatorname{Eu_{Sr}^0}$)² is a $\operatorname{Eu_{Sr}^0}$ and $\operatorname{U_{Sr}^0}$; ($\operatorname{Eu_{Sr}^0}$)² is a $\operatorname{U_$ $\mathrm{Sr}_i)^+$ is a complex of $\mathrm{Eu}_{\mathrm{Sr}}^0$ and Sr_i^+ , and $(\mathrm{Eu}_{\mathrm{Sr}}\mathrm{-Sr}_i)^0$ is a complex of $\mathrm{Eu}_{\mathrm{Sr}}^0$ and Sr_i^0 . Note that we determine the charge state of a defect configuration by examining the calculated total and local magnetic moments, electron occupation, and local lattice environment. The (+/0) level of Eu_{Sr}-Dy_{Sr} is 6.11 eV above the VBM, almost the same as that of the isolated Dy_{Sr}; the (2 + /+) and (+/0) levels of Eu_{Sr} - Sr_i are 6.04 eV and 6.21 eV above the VBM, almost the same as those of the isolated Sr_i .

Most notably, we find that the binding energy of the

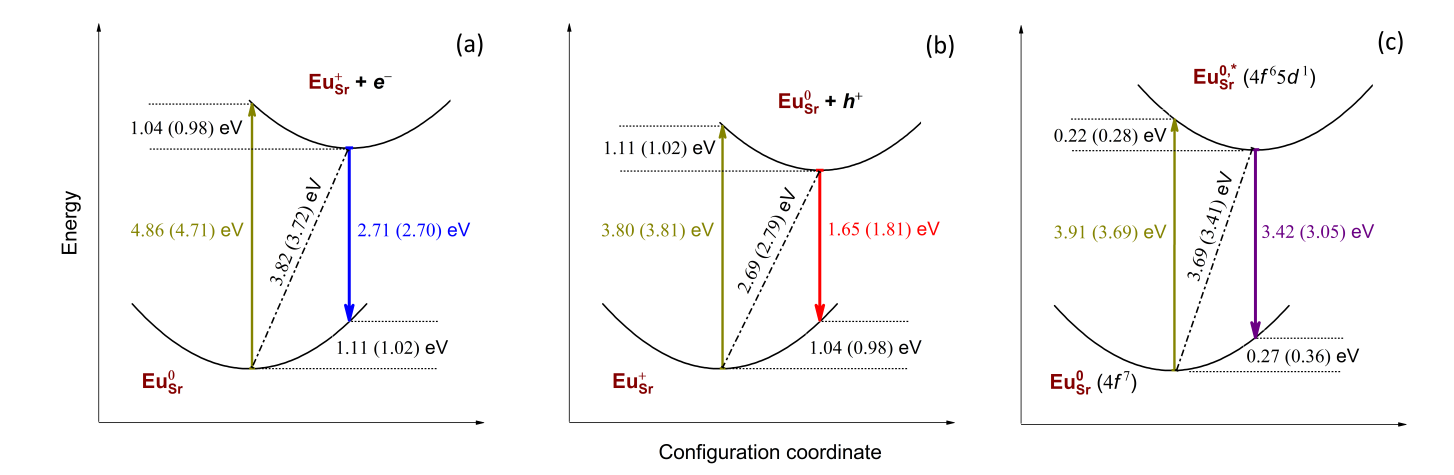


FIG. 8. Configuration-coordinate diagram illustrating optical absorption (up arrow) and emission (down arrow) processes for Eu_{Sr} in $SrAl_2O_4$: band–defect transitions involving the (+/0) defect level of Eu_{Sr} exchanging (a) electrons with the CBM or (b) holes with the VBM, and (c) interconfigurational 5d–4f transitions in Eu_{Sr}^0 . The dash-dotted line indicates the thermal energy (i.e., ZPL). The values sandwiched between two dotted lines are the relaxation energies (i.e., the Franck-Condon shifts). The values outside (inside) the brackets are for Eu at the Sr1 (Sr2) lattice site. Axes are not to scale.

Eu-related complexes is very small or even negative, see Table III, indicating that they are not stable under thermodynamic equilibrium, which is also consistent with the above analysis of the electronic behavior. In other words, $\rm Eu_{Sr}$ is unlikely to stay close and form a defect complex with $\rm Dy_{Sr}$ or any of the dominant native defects in $\rm SrAl_2O_4$, and even if it does, e.g., when the constituent defects get trapped next to each other, the electronic behavior of the complex in the relevant range of Fermilevel values is not that different from the isolated constituents. Our results for $\rm Eu_{Sr}\text{-}Dy_{Sr}$ are thus consistent with experimental observations that, in $(\rm Eu^{2+}, \rm RE^{3+})$ -doped $\rm SrAl_2O_4$, the $\rm RE^{3+}$ co-dopant only enhances the afterglow time and intensity and does not change the position or the shape of the emission band [5, 51].

D. Eu-related optical transitions

Let us now examine possible band–defect and interconfigurational 5d-4f optical transitions involving the Eu_{Sr} defect (The intraconfigurational Eu 4f-4f optical transitions are not explicitly considered in this work).

Figure 8(a) illustrates the optical absorption (defect-to-band) and emission (band-to-defect) processes involving the (+/0) level of Eu_{Sr} exchanging electrons with the CBM. Under illumination, for example, the Eu_{Sr} configuration (e.g., present in as-prepared Eu-doped SrAl₂O₄ samples) can absorb a photon and become ionized to Eu_{Sr} with the removed electron being excited into the conduction band. The peak absorption energy ($E_{\rm abs}$) related to the optical transition level $E_{\rm opt}^{0/+}$ (the formation energy difference between Eu_{Sr} and the Eu_{Sr} configuration in the lattice geometry of Eu_{Sr}) is 4.86 eV (4.71 eV), with a relaxation energy (i.e., the Franck-Condon shift, $d_{\rm FC}^{\rm e}$)

of 1.04 eV (0.98 eV), when Eu is incorporated at the Sr1 (Sr2) lattice site. With such a large relaxation energy, the emission is expected to be broad. In the reverse process, Eu_{Sr} can capture an electron from the CBM, e.g., previously excited from Eu_{Sr}^0 (or from the valence band) to the conduction band. If the recombination is radiative, a photon will be emitted. The peak emission energy $(E_{\rm em})$ related to the optical transition level $E_{\rm opt}^{+/0}$ (the formation energy difference between Eu_{Sr} and the Eu_{Sr}⁰ configuration in the lattice geometry of $\mathrm{Eu}_{\mathrm{Sr}}^+$) is 2.71 eV (2.70 eV), with a relaxation energy $(d_{\text{FC}}^{\text{g}})$ of 1.11 eV (1.02 eV)eV), at the Sr1 (Sr2) site. The thermal energy (E_{therm} ; also referred to as the zero-phonon line or ZPL) associated with the $Eu_{Sr}^0 \rightleftharpoons Eu_{Sr}^+ + e^-$ transitions is 3.38 eV (3.25 eV) at the Sr1 (Sr2) site, measured from the CBM. The ZPL marks the initial *onset* of the absorption band.

Note, however, that the band-to-defect emission process $\mathrm{Eu}_{\mathrm{Sr}}^+ + e^- \to \mathrm{Eu}_{\mathrm{Sr}}^0$ may not occur at all due to another, competing process in which the recombination is nonradiatively: $\mathrm{Eu}_{\mathrm{Sr}}^+ + e^- \to \mathrm{Eu}_{\mathrm{Sr}}^{0,*}$, where $\mathrm{Eu}_{\mathrm{Sr}}^{0,*}$ is Eu^{2+} in its excited state $4f^65d^1$. In this case, $\mathrm{Eu}_{\mathrm{Sr}}^{0,*}$ will relax to its ground state $\mathrm{Eu}_{\mathrm{Sr}}^0$ and release a photon through the allowed 5d–4f transition (discussed below).

In addition to exchanging electrons with the CBM, the (+/0) level of Eu_{Sr} can also exchange holes with the VBM. Figure 8(b) illustrates the absorption and emission Eu_{Sr} \rightleftharpoons Eu_{Sr} + h^+ processes. In the literature, these processes are often regarded as involving an O²⁻ to Eu³⁺ charge transfer (CT) and referred to as CT processes [13, 19]. The hole (h^+) state at the VBM consists primarily of the O 2p states, as discussed earlier. Our calculations show a different set of the absorption, emission, relaxation, and thermal energies as indicated in Fig. 8(b). Similar to the earlier case, the band-to-defect emission Eu_{Sr} + $h^+ \rightarrow$ Eu_{Sr} may not be observed. This

is because the energy from the recombination of the electron localized at $\mathrm{Eu}_{\mathrm{Sr}}^0$ and the free hole can quickly be absorbed into the 4f-electron core of Eu^{3+} which then excites the ion and leads to intra-f luminescence, as previously discussed in the case of RE-doped GaN [52].

Experimentally, Botterman et al. [15] reported a broad excitation band peaking at 276 nm (4.49 eV); Zollfrank et al. [13] and Bierwagen et al. [14] reported a similar value, at 250 nm (4.96 eV). This band has often been assigned to an O^{2-} to Eu^{3+} charge transfer [13], which corresponds to the $Eu^{+}_{Sr} \rightarrow Eu^{0}_{Sr} + h^{+}$ process $[E_{abs} = 3.80 \text{ or } 3.81 \text{ eV}; \text{ Fig. 8(b)}]$ in our work. On the basis of our results, however, that excitation band should instead be assigned to the $Eu^{0}_{Sr} \rightarrow Eu^{+}_{Sr} + e^{-}$ process $[E_{abs} = 4.86 \text{ or } 4.71 \text{ eV}; \text{Fig. 8(a)}]$. Note that there have been no reports of broad CT emission bands; and only sharp 4f-4f transitions are observed in the emission spectrum of Eu^{3+} in $SrAl_2O_4$ [14, 15]. This appears to be consistent with our discussion regarding alternative emission processes.

Figure 8(c) illustrates similar processes, but now involving the electric-dipole allowed 5d-4f transitions in the neutral defect configuration Eu_{Sr}^0 and with the energies obtained from constrained occupancy HSE calculations. In the absorption process, Eu_{Sr}^0 (4 f^7) absorbs a photon and becomes $\operatorname{Eu}_{\operatorname{Sr}}^{0,*}(4f^65d^1)$ with an electron being excited to a higher lying level which is the lowest Eu $5d^1$ state (that is now pushed down from the conduction band due to the occupation of the excited electron). The peak absorption energy related to the $4f^7 \to 4f^65d^{\dot{1}}$, i.e., the total-energy difference between Eu $_{\rm Sr}^0$ ($4f^7$) and the excited configuration $\operatorname{Eu}_{\operatorname{Sr}}^{0,*}(4f^65d^1)$ in the lattice geometry of the former, is 3.91 eV (3.69 eV), with a relaxation energy $d_{FC}^{e} = 0.22 \text{ eV} (0.28 \text{ eV})$, when Eu is incorporated at the Sr1 (Sr2) site. The ZPL, 3.69 eV (3.41 eV) at the Sr1 (Sr2) site, is the total-energy difference between the ground state $4f^7$ [Fig. 13(a)] and the excited state $4f^65d^1$ [Fig. 13(b)]. In the reverse process, the excited electron recombines radiatively with the hole that has been left behind and emits a photon. The peak emission energy related to the $4f^65d^1 \rightarrow 4f^7$ process, i.e., the total-energy difference between the excited $\mathrm{Eu}_{\mathrm{Sr}}^{0,*}$ $(4f^65d^1)$ and the ground state $\mathrm{Eu}_{\mathrm{Sr}}^0$ $(4f^7)$ in the lattice geometry of the former, is 3.42 eV (3.05 eV), with a relaxation energy $d_{\rm FC}^{\rm g}=0.27$ eV (0.36 eV), when Eu is at the Sr1 (Sr2) site. The Stokes shift, $\Delta S=d_{\rm FC}^{\rm e}+d_{\rm FC}^{\rm g}$, is calculated to be 0.49 (0.64) eV at the Sr1 (Sr2) site.

Although there are differences between our calculated energies for the $4f^7 \rightleftharpoons 4f^65d^1$ processes (summarized in Table IV) and those obtained in experiments, the emissions at the Sr1 and Sr2 lattice sites can be identified with the two broad emission bands peaking at 445 nm (2.79 eV, blue) and 520 nm (2.38 eV, green) and the Stokes shifts of roughly 3000 cm⁻¹ (0.37 eV) and 4000 cm⁻¹ (0.50 eV), respectively, observed in Eu²⁺-doped SrAl₂O₄ [12, 15, 53]. We find that the difference between the two emission energies is 0.37 eV, just like in experiments (which is larger than that for the band–defect optical transitions discussed earlier, thus indicating the 5d–4f

transitions are more sensitive to the local lattice environments). The calculated peak emission energy and Stokes shift are higher than the reported experimental values by 0.63 eV (0.67 eV) and 0.12 eV (0.14 eV) at the Sr1 (Sr2) site, respectively, which is an almost constant shift among the two lattice sites. The discrepancies with experiments may be ascribed to the electron–hole interaction that is not included in the constrained occupancy approach we employ to describe the excited state of Eu^{2+} .

Note that, using constrained occupancy DFT+U calculations, Jia et al. [34] reported much lower values for the emission energies. For example, they obtained 2.316 (2.547) eV at the Sr1 (Sr2) site and assigned the experimentally observed green and blue luminescence bands to the Sr1 and Sr2 sites, respectively, which is different from our assignment and that of Ning et al. [54] based on multiconfigurational and constrained occupancy calculations. Our attempts to reproduce the results of Jia et al. [34] using a similar computational setup are not successful. Specifically, in our calculations based on DFT+U[55] with U = 7.5 eV applied on the Eu 4f states, a $1\times1\times2$ (56-atom) supercell, and a $3\times3\times3$ k-point mesh, we find the emission energy is 3.52 (3.38) eV at the Sr1 (Sr2) site, which shows the same trend as in our HSEbased calculations discussed earlier; see also Table IV.

E. Carrier traps for persistent luminescence

Let us now identify charge carrier traps that can play a role in the persistent luminescence of $\mathrm{Eu^{2+}}$ -doped $\mathrm{SrAl_2O_4}$. Among the native point defects, we find that Sr_i can act as a trapping center for electrons. Being stable as Sr_i^{2+} in as-prepared $\mathrm{SrAl_2O_4}$, the defect can capture up to two electrons. The thermodynamic transition levels (2+/+) and (+/0) of Sr_i , at 0.44 eV and 0.30 eV below the CBM, respectively, are sufficient close to the CBM, and the positively charged carrier-capturing configurations, i.e., Sr_i^{2+} and Sr_i^+ , are electrostatically attractive to electrons from the conduction band.

Note that, in general, the carrier capture cross section increases by orders of magnitude in going from Coulomb repulsive defect centers to neutral centers to attractive centers [56]. Also note that the error bar in our calculations of the transitions levels, $\epsilon(q/q')$ and $E_{\rm opt}^{q/q'}$, is about 0.1 eV. A discrepancy of about 0.2 eV should be expected in a comparison between the calculated and the experimental values when the energy levels are measured from the CBM; here, the additional 0.1 eV is to take into account a possible difference between the calculated and the actual band gaps and/or measurement uncertainties.

The presence of the Sr_i -related trapping centers can explain why the emission observed in Eu^{2+} -doped $SrAl_2O_4$ is persistent (albeit with a short afterglow time) even without Dy^{3+} co-doping [5, 11, 57, 58]. Notably, our results indicate that oxygen vacancies cannot act as efficient electron traps for room-temperature persistent luminescence (even when they occur with a high concentra-

tion, e.g., in samples prepared under reducing conditions) as their defect levels are too deep in the host band gap.

Finally, with the (+/0) level located at 0.30 (0.38) eV below the CBM at the Sr1 (Sr2) site as reported earlier, $\mathrm{Dy_{Sr}}$ can be an efficient electron trap. The electroncapturing configuration, Dy_{Sr}⁺, is positively charged. Note that, unlike Sr_i where the defect state associated with Sr_i^+ and Sr_i^0 (i.e., Sr_i^{2+} after capturing one and two electrons, respectively) is derived largely from the host states at the CBM and delocalized over several lattice sites, that associated with $\mathrm{Dy}_\mathrm{Sr}^0$ (i.e., $\mathrm{Dy}_\mathrm{Sr}^+$ after capturing an electron) is highly localized Dy 5d states. This indicates that the Dy_{Sr}-related traps are much more stable than the Sr_i-related ones, which is consistent with the fact that the performance of the afterglow in Eu^{2+} doped SrAl₂O₄ is significantly improved by Dy co-doping [51, 58, 59]. First-principles calculations of photoionization and carrier capture rates [60, 61] can provide a more quantitative understanding. Also note that the presence of the $(Sr_i \text{ and } Dy_{Sr} \text{ related})$ electron traps is consistent with the fact that the Eu²⁺ $4f^65d^1 \rightarrow 4f^7$ emission was observed to be quenched via the conduction band [62].

IV. CONCLUSIONS

We have carried out a comprehensive study of native point defects and rare-earth (co)dopants in $SrAl_2O_4$. The major conclusions can be summarized as follows:

- 1. Eu is mixed valence of $\mathrm{Eu^{2+}}$ and $\mathrm{Eu^{3+}}$ and energetically most favorable at the Sr sites. The $\mathrm{Eu^{2+}}/\mathrm{Eu^{3+}}$ ratio can be tuned by tuning the synthesis conditions. Similarly, both $\mathrm{Dy^{2+}}$ and $\mathrm{Dy^{3+}}$ can be stabilized and are energetically most favorable at the Sr sites. $\mathrm{Dy^{2+}}$ is, however, always energetically much less favorable than $\mathrm{Dy^{3+}}$ and thus would not be realized in synthesis, although it can be photogenerated under irradiation.
- 2. Band–defect and interconfigurational 5d–4f optical transitions involving the Eu_{Sr} defect are investigated using first-principles defect calculations and a constrained occupancy approach, and alternative processes are discussed. On the basis of our results, we assign the broad blue (445 nm) and green (520 nm) emission bands observed in Eu²⁺-doped SrAl₂O₄ to the Eu²⁺ 4f⁶⁵d¹ \rightarrow 4f⁷ transition at the Sr1 and Sr2 sites, respectively.
- 3. Strontium interstitials are found to be efficient electron traps for room-temperature persistent luminescence. When the material is co-doped with Dy, the co-dopant

provides an even more stable electron trapping center due to the stabilization of Dy^{2+} which can explain the significantly improved performance of the afterglow in (Eu,Dy)-doped samples. Oxygen vacancies cannot be efficient electron traps, in contrast to what is commonly believed, due to their very deep defect levels.

Our work thus calls for a re-assessment of certain assumptions regarding specific defects previously made in all the mechanisms proposed for the persistent luminescence observed in Eu- and (Eu,Dy)-doped $\rm SrAl_2O_4$. It also shows a need to go beyond a constrained occupancy approach in order to obtain more quantitative results for the interconfigurational 5d-4f optical transitions.

ACKNOWLEDGMENTS

The author gratefully acknowledges Stéphane Jobic (Nantes Université, CNRS) for helpful discussion. This work used resources of the Center for Computationally Assisted Science and Technology (CCAST) at North Dakota State University, which were made possible in part by NSF MRI Award No. 2019077.

Appendix A: Supporting figures and tables

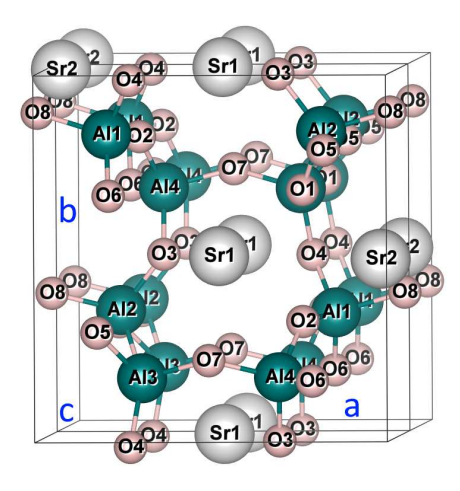


FIG. 9. Crystal structure of monoclinic $SrAl_2O_4$ (space group $P2_1$). The unit cell is doubled along the c-axis to show the Sr1 and Sr2 channels. Large (gray) spheres are Sr, medium (blue) are Al, and small (red) are O.

^[1] P. F. Smet, K. Van den Eeckhout, O. Q. De Clercq, and D. Poelman, Persistent phosphors, in *Handbook on the Physics and Chemistry of Rare Earths*, Handbook on the Physics and Chemistry of Rare Earths, Vol. 48, edited by J.-C. Bünzli and V. K. Pecharsky (Elsevier, 2015) pp. 1–108.

^[2] J. Xu and S. Tanabe, Persistent luminescence instead of phosphorescence: History, mechanism, and perspective, J. Lumin. 205, 581 (2019).

^[3] D. Poelman, D. Van der Heggen, J. Du, E. Cosaert, and P. F. Smet, Persistent phosphors for the future: Fit for the right application, J. Appl. Phys. 128, 240903 (2020).

- [4] Y. Murayam, N. Takeuchi, Y. Aoki, and T. Matsuzawa, Phosphorescent phosphor (1994), EP0622440.
- [5] T. Matsuzawa, Y. Aoki, N. Takeuchi, and Y. Murayama, A New Long Phosphorescent Phosphor with High Brightness, SrAl₂O₄:Eu²⁺,Dy³⁺, J. Electrochem. Soc. 143, 2670 (1996).
- [6] R. E. Rojas-Hernandez, F. Rubio-Marcos, M. Ángel Rodriguez, and J. F. Fernandez, Long lasting phosphors: SrAl₂O₄:Eu,Dy as the most studied material, Renew. Sustain. Energy Rev. 81, 2759 (2018).
- [7] V. Vitola, D. Millers, I. Bite, K. Smits, and A. Spustaka, Recent progress in understanding the persistent luminescence in SrAl₂O₄:Eu,Dy, Mater. Sci. Tech. 35, 1661 (2019).
- [8] H. H.-R. Hagemann and J. Afshani, Synthesis, luminescence and persistent luminescence of europium-doped strontium aluminates, in Handbook on the Physics and Chemistry of Rare Earths, Handbook on the Physics and Chemistry of Rare Earths, Vol. 60, edited by J.-C. G. Bünzli and V. K. Pecharsky (Elsevier, 2021) pp. 163–225.
- [9] F. C. Palilla, A. K. Levine, and M. R. Tomkus, Fluorescent Properties of Alkaline Earth Aluminates of the Type MAl₂O₄ Activated by Divalent Europium, J. Electrochem. Soc. 115, 642 (1968).
- [10] G. Blasse and A. Bril, Flourescence of Eu²⁺-activated alkaline-earth aluminates, Philips Res. Rep. 23, 201 (1968).
- [11] V. Abbruscato, Optical and Eelectrical Properties of SrAl₂O₄:Eu²⁺, J. Electrochem. Soc. 118, 930 (1971).
- [12] S. H. M. Poort, W. P. Blokpoel, and G. Blasse, Luminescence of Eu²⁺ in barium and strontium aluminate and gallate, Chem. Mater. 7, 1547 (1995).
- [13] C. Zollfrank, S. Gruber, M. Batentschuk, A. Osvet, F. Goetz-Neunhoeffer, S. Dittrich, J. Grabow, H.-D. Kurland, and F. Müller, Synthesis of Eu-doped SrAl₂O₄ nanophosphors by CO₂ laser vaporization, Acta Mater. 61, 7133 (2013).
- [14] J. Bierwagen, T. Delgado, J. Afshani, S. Yoon, N. Gartmann, B. Walfort, and H. Hagemann, Observation of multiple sites for trivalent europium ions in SrAl₂O₄, J. Lumin. 239, 118348 (2021).
- [15] J. Botterman, J. J. Joos, and P. F. Smet, Trapping and detrapping in $SrAl_2O_4$:Eu,Dy persistent phosphors: Influence of excitation wavelength and temperature, Phys. Rev. B **90**, 085147 (2014).
- [16] C. Beauger, Élaboration, caractérisation et modélisation des phénomènes de luminescence du monoaluminate de strontium dopé à l'europium et au dysprosium SrAl₂O₄: Eu, Dy, Ph.D. thesis, Ecole Nationale Supérieure des Mines de Saint-Etienne (1999).
- [17] T. Aitasalo, P. Dereń, J. Hölsä, H. Jungner, J.-C. Krupa, M. Lastusaari, J. Legendziewicz, J. Niittykoski, and W. Stręk, Persistent luminescence phenomena in materials doped with rare earth ions, J. Solid State Chem. 171, 114 (2003).
- [18] T. Aitasalo, J. Hölsä, H. Jungner, J.-C. Krupa, M. Lastusaari, J. Legendziewicz, and J. Niittykoski, Effect of temperature on the luminescence processes of SrAl₂O₄:Eu²⁺, Radiat. Meas. 38, 727 (2004).
- [19] F. Clabau, X. Rocquefelte, S. Jobic, P. Deniard, M.-H. Whangbo, A. Garcia, and T. Le Mercier, Mechanism of Phosphorescence Appropriate for the Long-Lasting Phos-

- phors Eu^{2+} -Doped $SrAl_2O_4$ with Codopants Dy^{3+} and B^{3+} , Chem. Mater. 17, 3904 (2005).
- [20] P. Dorenbos, Mechanism of Persistent Luminescence in Eu²⁺ and Dy³⁺ Codoped Aluminate and Silicate Compounds, J. Electrochem. Soc. 152, H107 (2005).
- [21] V. Liepina, D. Millers, and K. Smits, Tunneling luminescence in long lasting afterglow of SrAl₂O₄:Eu,Dy, J. Lumin. 185, 151 (2017).
- [22] P. Zeng, X. Wei, M. Yin, and Y. Chen, Investigation of the long afterglow mechanism in SrAl₂O₄:Eu²⁺/Dy³⁺ by optically stimulated luminescence and thermoluminescence, J. Lumin. 199, 400 (2018).
- [23] J. R. N. Gnidakouong and G. J. Yun, Dislocation density level induced divergence between stress-free afterglow and mechanoluminescence in SrAl₂O₄: Eu²⁺, Dy³⁺, Ceram. Int. 45, 1794 (2019).
- [24] J. Heyd, G. E. Scuseria, and M. Ernzerhof, Hybrid functionals based on a screened Coulomb potential, J. Chem. Phys. 118, 8207 (2003).
- [25] C. Freysoldt, B. Grabowski, T. Hickel, J. Neugebauer, G. Kresse, A. Janotti, and C. G. Van de Walle, First-principles calculations for point defects in solids, Rev. Mod. Phys. 86, 253 (2014).
- [26] K. Hoang, Hybrid density functional study of optically active Er³⁺ centers in GaN, Phys. Status Solidi RRL 9, 722 (2015).
- [27] K. Hoang, First-principles identification of defect levels in Er-doped GaN, Phys. Status Solidi RRL 10, 915 (2016).
- [28] K. Hoang, Tuning the valence and concentration of europium and luminescence centers in GaN through co-doping and defect association, Phys. Rev. Materials 5, 034601 (2021).
- [29] C. G. Van de Walle and J. Neugebauer, First-principles calculations for defects and impurities: Applications to III-nitrides, J. Appl. Phys. 95, 3851 (2004).
- [30] C. Freysoldt, J. Neugebauer, and C. G. Van de Walle, Fully Ab Initio Finite-Size Corrections for Charged-Defect Supercell Calculations, Phys. Rev. Lett. 102, 016402 (2009).
- [31] C. Freysoldt, J. Neugebauer, and C. G. Van de Walle, Electrostatic interactions between charged defects in supercells, phys. status solidi (b) 248, 1067 (2011).
- [32] G. Blasse and B. C. Grabmaier, Luminescent Materials (Springer-Verlag, Berlin, 1994).
- [33] A. Canning, A. Chaudhry, R. Boutchko, and N. Grønbech-Jensen, First-principles study of luminescence in Ce-doped inorganic scintillators, Phys. Rev. B 83, 125115 (2011).
- [34] Y. Jia, A. Miglio, S. Poncé, M. Mikami, and X. Gonze, First-principles study of the luminescence of Eu²⁺-doped phosphors, Phys. Rev. B 96, 125132 (2017).
- [35] P. E. Blöchl, Projector augmented-wave method, Phys. Rev. B 50, 17953 (1994).
- [36] G. Kresse and J. Furthmüller, Efficient iterative schemes for ab initio total-energy calculations using a plane-wave basis set, Phys. Rev. B 54, 11169 (1996).
- [37] A. R. Schulze and M. Buschbaum, Zur Verbindungsbildung von MeO:M₂O₃. IV. Zur Struktur von monoklinem SrAl₂O₄, Z. Anorg. Allg. Chem. 475, 205 (1981).
- [38] J. Holsa, T. Laamanen, M. Lastusaari, J. Niittykoski, and P. Novak, Electronic structure of the SrAl₂O₄:Eu²⁺ persistent luminescence material, J. Rare Earths 27, 550 (2009).
- [39] D. Dutczak, T. Jüstel, C. Ronda, and A. Mei-

- jerink, $\mathrm{Eu^{2+}}$ luminescence in strontium aluminates, Phys. Chem. Chem. Phys. **17**, 15236 (2015).
- [40] M. Gajdoš, K. Hummer, G. Kresse, J. Furthmüller, and F. Bechstedt, Linear optical properties in the projector-augmented wave methodology, Phys. Rev. B 73, 045112 (2006).
- [41] J. P. Perdew, K. Burke, and M. Ernzerhof, Generalized gradient approximation made simple, Phys. Rev. Lett. 77, 3865 (1996).
- [42] A. Jain, S. P. Ong, G. Hautier, W. Chen, W. D. Richards, S. Dacek, S. Cholia, D. Gunter, D. Skinner, G. Ceder, and K. A. Persson, Commentary: The materials project: A materials genome approach to accelerating materials innovation, APL Materials 1, 011002 (2013).
- [43] F. Massazza, The system SrO-Al₂O₃, Chim. Ind. (Milan) 41, 108 (1959).
- [44] M. Capron and A. Douy, Strontium Dialuminate SrAl₄O₇: Synthesis and Stability, J. Am. Ceram. Soc. 85, 3036 (2002).
- [45] D. R. Stull and H. Prophet, JANAF Thermochemical Tables, 2nd ed. (U.S. National Bureau of Standards, Washington, D.C., 1971).
- [46] K. Momma and F. Izumi, VESTA 3 for three-dimensional visualization of crystal, volumetric and morphology data, J. Appl. Cryst. 44, 1272 (2011).
- [47] E. Finley, A. Mansouri Tehrani, and J. Brgoch, Intrinsic Defects Drive Persistent Luminescence in Monoclinic SrAl₂O₄:Eu²⁺, J. Phys. Chem. C 122, 16309 (2018).
- [48] G. Kaur Behrh, H. Serier-Brault, S. Jobic, and R. Gautier, A Chemical Route Towards Single-Phase Materials with Controllable Photoluminescence, Angew. Chem. Intl. Ed. 54, 11501 (2015).
- [49] D. Wang, Q. Yin, Y. Li, and M. Wang, Concentration quenching of Eu²⁺ in SrO·Al₂O₃:Eu²⁺ phosphor, J. Lumin. 97, 1 (2002).
- [50] J. J. Joos, K. Korthout, L. Amidani, P. Glatzel, D. Poelman, and P. F. Smet, Identification of Dy³⁺/Dy²⁺ as Electron Trap in Persistent Phosphors, Phys. Rev. Lett. **125**, 033001 (2020).
- [51] T. Katsumata, S. Toyomane, R. Sakai, S. Komuro, and T. Morikawa, Trap Levels in Eu-Doped SrAl₂O₄ Phosphor Crystals Co-Doped with Rare-Earth Elements, J. Am. Ceram. Soc. 89, 932 (2006).
- [52] K. Hoang, Rare-earth defects in GaN: A sys-

- tematic investigation of the lanthanide series, Phys. Rev. Materials **6**, 044601 (2022).
- [53] J. Bierwagen, S. Yoon, N. Gartmann, B. Walfort, and H. Hagemann, Thermal and concentration dependent energy transfer of Eu²⁺ in SrAl₂O₄, Opt. Mater. Express 6, 793 (2016).
- [54] L. Ning, X. Huang, Y. Huang, and P. A. Tanner, Origin of the green persistent luminescence of Eu-doped $SrAl_2O_4$ from a multiconfigurational ab initio study of $4f^7 \rightarrow 4f^65d^1$ transitions, J. Mater. Chem. C **6**, 6637 (2018).
- [55] V. I. Anisimov, J. Zaanen, and O. K. Andersen, Hubbard-corrected density-functional theory, Phys. Rev. B 44, 943 (1991).
- [56] J. W. Mayer and S. S. Lau, Electronic Materials Science: For Integrated Circuits in Si and GaAs (MacMillan Publishing, New York, 1990) p. 161.
- [57] X. Lu, W. Shu, Q. Yu, Q. Fang, and X. Xiong, Roles of doping ions in persistent luminescence of SrAl₂O₄: Eu²⁺,RE³⁺ phosphors, Glass Phys. Chem. 33, 62 (2007).
- [58] J. Bierwagen, T. Delgado, G. Jiranek, S. Yoon, N. Gartmann, B. Walfort, M. Pollnau, and H. Hagemann, Probing traps in the persistent phosphor SrAl₂O₄:Eu²⁺,Dy³⁺,B³⁺ - A wavelength, temperature and sample dependent thermoluminescence investigation, J. Lumin. 222, 117113 (2020).
- [59] E. Nakazawa, Y. Murazaki, and S. Saito, Mechanism of the persistent phosphorescence in Sr₄Al₁₄O₂₅:Eu and SrAl₂O₄:Eu codoped with rare earth ions, J. Appl. Phys. **100**, 113113 (2006).
- [60] L. Razinkovas, M. Maciaszek, F. Reinhard, M. W. Doherty, and A. Alkauskas, Photoionization of negatively charged NV centers in diamond: Theory and *ab initio* calculations, Phys. Rev. B 104, 235301 (2021).
- [61] C. E. Dreyer, A. Alkauskas, J. L. Lyons, and C. G. Van de Walle, Radiative capture rates at deep defects from electronic structure calculations, Phys. Rev. B 102, 085305 (2020).
- [62] J. Ueda, T. Nakanishi, Y. Katayama, and S. Tanabe, Optical and optoelectronic analysis of persistent luminescence in Eu²⁺-Dy³⁺ codoped SrAl₂O₄ ceramic phosphor, phys. stat. solidi c 9, 2322 (2012).

TABLE I. Formation enthalpies (calculated at 0 K, in eV per formula unit) of SrAl₂O₄, Sr–Al–O phases that define the stability region of SrAl₂O₄, and Eu- and Dy-related phases employed in the determination of the Eu and Dy chemical potentials.

SrAl ₂ O ₄	Sr ₃ Al ₂ O ₆	$Sr_4Al_{14}O_{25}$	SrO_2	$SrAl_2$	$SrAl_4$	Eu_2O_3	EuO	$\mathrm{Dy_2O_3}$
-22.6974	-34.2968	-139.7826	-5.8455	-0.8403	-1.2252	-14.3794	-6.2000	-18.7462

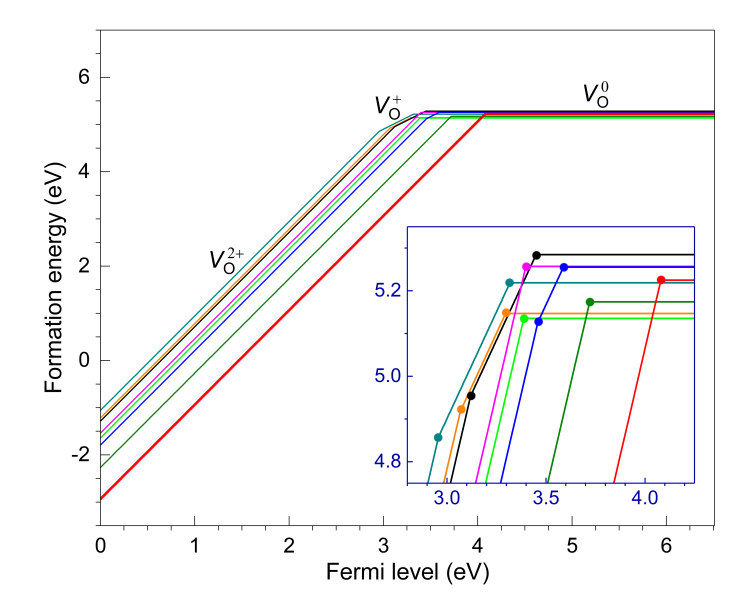


FIG. 10. Formation energies of oxygen vacancies at eight inequivalent O lattice sites in $SrAl_2O_4$ (see Fig. S1), as a function of the Fermi level from the VBM to the CBM, calculated at point O1 in the phase diagram (Fig. 1). For each defect, only segments of the formation energy lines corresponding to the lowest-energy charge states are shown. The kinks connecting two energy segments with different slopes mark the defect levels [i.e., thermodynamic transition levels $\epsilon(q/q')$]. The defect levels introduced by the vacancies are 2.43–3.55 eV below the CBM. The lowest-energy V_0^{2+} configuration occurs at the O8 site.

TABLE II. Defect energy levels (in eV, with respect to the VBM) induced by native defects and rare-earth (RE) impurities.

Defect	Lattice site	Stable RE ions	Defect energy levels
$V_{\rm O}$	O8 site		$\epsilon(2+/0) = 4.08$
O_i			$\epsilon(+/0) = 1.29, \ \epsilon(0/2-) = 3.29^a$
$V_{ m Sr}$	Sr1 site		$\epsilon(+/0) = 0.95, \ \epsilon(0/-) = 1.21, \ \epsilon(-/2-) = 1.73$
	Sr2 site		$\epsilon(+/0) = 0.94, \ \epsilon(0/-) = 1.24, \ \epsilon(-/2-) = 1.73$
Sr_i	Sr1 channel		$\epsilon(3+/2+) = 0.61, \ \epsilon(2+/+) = 6.00, \ \epsilon(+/0) = 6.17$
	Sr2 channel		$\epsilon(3+/2+) = 0.65, \ \epsilon(2+/+) = 6.08, \ \epsilon(+/0) = 6.21$
$\mathrm{Al}_{\mathrm{Sr}}$	Sr2 site		$\epsilon(2+/+) = 0.24, \ \epsilon(+/-) = 5.10^b$
$\mathrm{Sr}_{\mathrm{Al}}$	Al2 site		$\epsilon(+/0) = 1.37, \ \epsilon(0/-) = 1.80$
$\mathrm{Eu_{Sr}}$	Sr1 site	${\rm Eu^{3+},Eu^{2+}}$	$\epsilon(+/0) = 2.69$
	Sr2 site	${\rm Eu^{3+}, Eu^{2+}}$	$\epsilon(+/0) = 2.79$
$\mathrm{Eu_{Al}}$	Al2 site	${\rm Eu^{3+}, Eu^{2+}}$	$\epsilon(2+/+) = 0.75, \ \epsilon(+/0) = 0.86, \ \epsilon(+/0) = 4.87$
$\mathrm{Dy_{Sr}}$	Sr1 site	Dy^{3+}, Dy^{2+}	$\epsilon(+/0) = 6.21$
-	Sr2 site	Dy^{3+}, Dy^{2+}	$\epsilon(+/0) = 6.13$
$\mathrm{Dy}_{\mathrm{Al}}$	Al2 site	Dy^{4+}, Dy^{3+}	$\epsilon(2+/+) = 0.60, \ \epsilon(+/0) = 1.07$

^aThe $\epsilon(0/-)$ and $\epsilon(-/2-)$ levels are very close to the $\epsilon(0/2-)$ level, at 3.28 and 3.30 eV, respectively.

^bThe $\epsilon(+/0)$ and $\epsilon(0/-)$ levels are very close to the $\epsilon(+/-)$ level, at 5.10 and 5.09 eV, respectively.

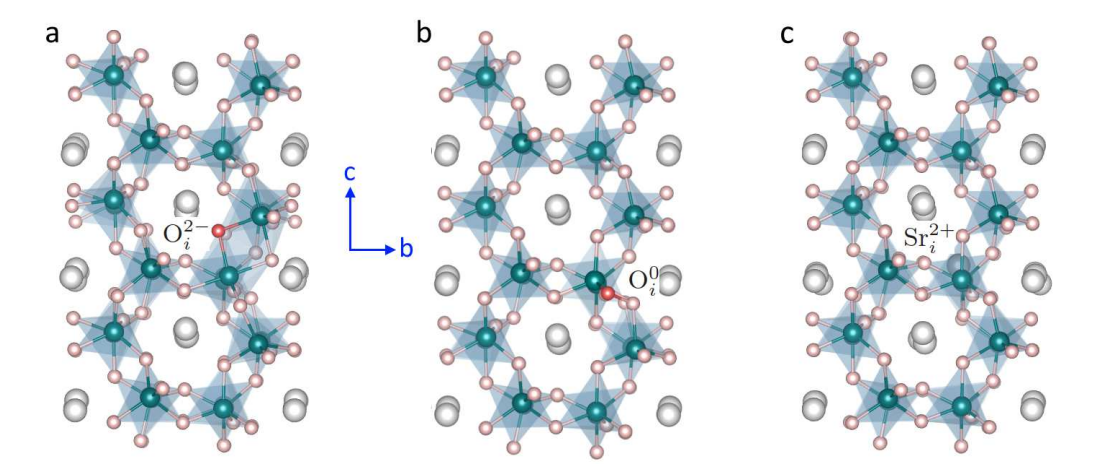


FIG. 11. A different view of (a) O_i^{2-} , (b) O_i^0 , and (c) Sr_i^{2+} (in the Sr2 channel; between two AlO₄ units when viewed along the a-axis) defect configurations in $SrAl_2O_4$. Large (gray) spheres are Sr, medium (blue) are Al, and small (red) are O.

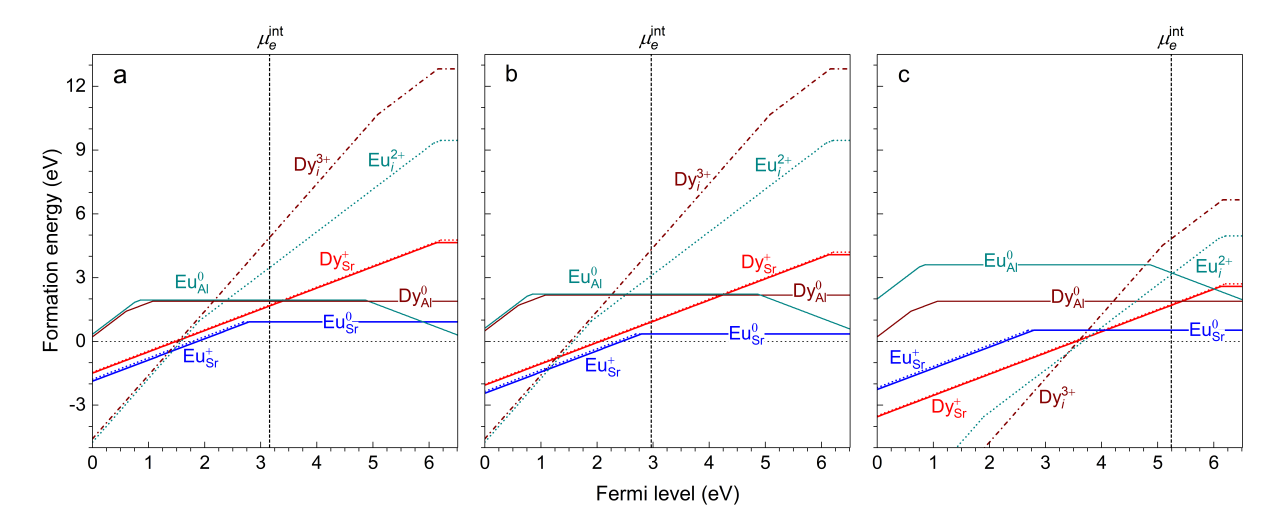


FIG. 12. Formation energies of Eu- and Dy-related defects in $SrAl_2O_4$, calculated at points (a) O1, (b) O2, and (c) R in the phase diagram (Fig. 1). The results for the Eu and Dy interstitials are also included. μ_e^{int} is the Fermi-level position determined by native point defects; see the main text. The kinks connecting two segments with different slopes mark the *defect levels*.

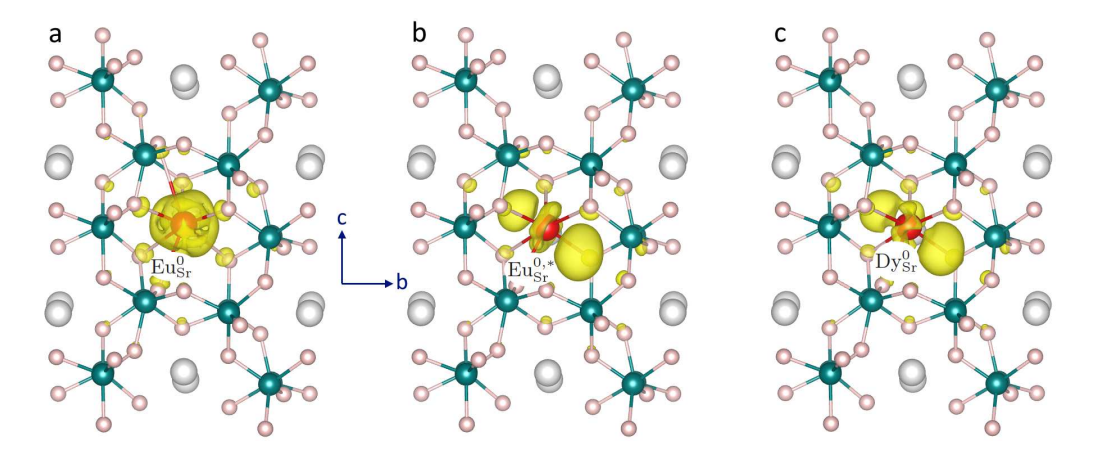


FIG. 13. Charge densities showing the localized electron residing at the highest occupied state of (a) $\mathrm{Eu_{Sr}^0}(4f^7)$, (b) $\mathrm{Eu_{Sr}^{0,*}}(4f^65d^1)$, and (c) $\mathrm{Dy_{Sr}^0}(4f^95d^1)$; all the three defect configurations are at the Sr2 site. The isovalue for the isosurface is set to 0.03 $e/\mathrm{\mathring{A}}^3$. Larger (red) spheres are $\mathrm{Eu/Dy}$, large (gray) are Sr, medium (blue) are Al, and small (red) are O.

TABLE III. Stable charge states	of Eu-related defect complex	es their constituent defects	and hinding energies (E.)
TABLE III. Stable charge states	s of rau-related defect complex	es, then constituent defects	. and dinding energies (7%).

Complex	Constituents	$E_{\rm b}~({\rm eV})$	Complex	Constituents	$E_{\rm b}~({\rm eV})$
$(Eu_{Sr}-Dy_{Sr})^{2+}$	$\mathrm{Eu}_{\mathrm{Sr}}^{+} + \mathrm{Dy}_{\mathrm{Sr}}^{+}$	-0.41	$(\mathrm{Eu_{Sr}}\text{-}\mathrm{Sr}_i)^{3+}$	$\mathrm{Eu}_{\mathrm{Sr}}^{+} + \mathrm{Sr}_{i}^{2+}$	-0.69
$(Eu_{Sr}-Dy_{Sr})^+$	$\mathrm{Eu}_{\mathrm{Sr}}^{0} + \mathrm{Dy}_{\mathrm{Sr}}^{+}$	-0.02	$(\mathrm{Eu_{Sr}}\text{-}\mathrm{Sr}_i)^{2+}$	$\mathrm{Eu}_{\mathrm{Sr}}^{0^{+}}+\mathrm{Sr}_{i}^{2+}$	0.01
$(\mathrm{Eu_{Sr}}\text{-}\mathrm{Dy_{Sr}})^0$	$\mathrm{Eu_{Sr}^0} + \mathrm{Dy_{Sr}^0}$	0.01	$(\mathrm{Eu}_{\mathrm{Sr}}\text{-}\mathrm{Sr}_{i})^{+}$	$\mathrm{Eu}_{\mathrm{Sr}}^{0} + \mathrm{Sr}_{i}^{+}$	0.05
$(\mathrm{Eu_{Sr}}\text{-}V_{\mathrm{O}})^{3+}$	$\mathrm{Eu}_{\mathrm{Sr}}^{+} + V_{\mathrm{O}}^{2+} \ \mathrm{Eu}_{\mathrm{Sr}}^{0} + V_{\mathrm{O}}^{2+}$	-0.73	$(\mathrm{Eu_{Sr}}\text{-}\mathrm{Sr}_i)^0$	$\mathrm{Eu}_{\mathrm{Sr}}^{0}+\mathrm{Sr}_{i}^{0}$	0.05
$(\mathrm{Eu_{Sr}}\text{-}V_{\mathrm{O}})^{2+}$	$Eu_{Sr}^{0} + V_{O}^{2+}$	0.07	$(\mathrm{Eu_{Sr}}\text{-}V_{\mathrm{Sr}})^+$	$\mathrm{Eu}_{\mathrm{Sr}}^{+} + V_{\mathrm{Sr}}^{0}$	0.31
$(\mathrm{Eu_{Sr}}\text{-}V_{\mathrm{O}})^{0}$	$\mathrm{Eu_{Sr}^0} + V_{\mathrm{O}}^{\mathrm{0}}$	0.01	$(\mathrm{Eu_{Sr}} ext{-}V_{\mathrm{Sr}})^0$	$\mathrm{Eu}_{\mathrm{Sr}}^+ + V_{\mathrm{Sr}}^-$	0.61
$(\mathrm{Eu}_{\mathrm{Sr}}\text{-}\mathrm{O}_{i})^{+}$	$\mathrm{Eu}_{\mathrm{Sr}}^{+} + \mathrm{O}_{i}^{0}$	-0.06	$(\mathrm{Eu_{Sr}}\text{-}V_{\mathrm{Sr}})^-$	$Eu_{Sr}^{+} + V_{Sr}^{2-}$	1.15
$(\mathrm{Eu_{Sr}}\text{-}\mathrm{O}_i)^-$	$ \begin{aligned} &\operatorname{Eu}_{\operatorname{Sr}}^{+} + \operatorname{O}_{i}^{2-} \\ &\operatorname{Eu}_{\operatorname{Sr}}^{0} + \operatorname{O}_{i}^{2-} \end{aligned} $	1.09	$(\mathrm{Eu_{Sr}}\text{-}V_{Sr})^{2-}$	$\mathrm{Eu_{Sr}^{0'}} + V_{Sr}^{2-}$	0.07
$(\mathrm{Eu_{Sr}}\text{-}\mathrm{O}_i)^{2-}$	$\mathrm{Eu}_{\mathrm{Sr}}^{0}+\mathrm{O}_{i}^{2-}$	0.00			

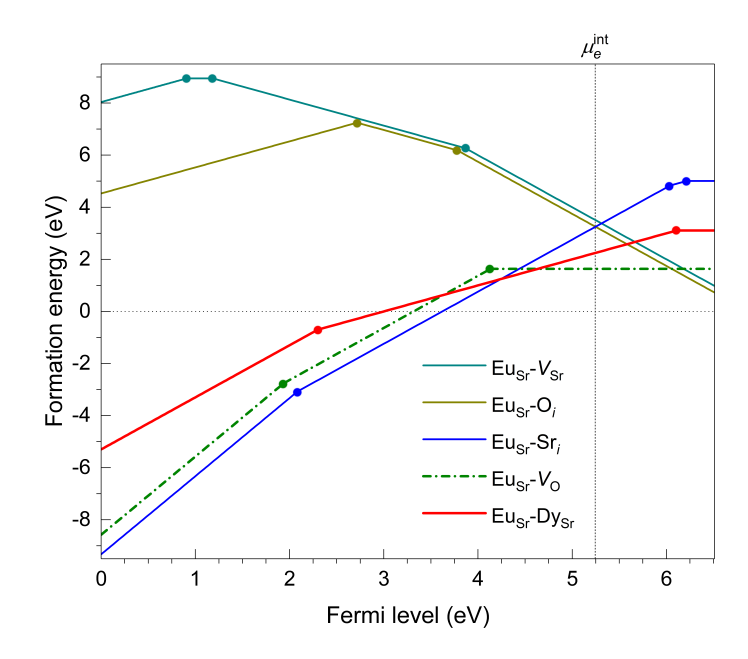


FIG. 14. Formation energies of possible Eu-related defect complexes in $SrAl_2O_4$, calculated at point R in the phase diagram (Fig. 1). The two constituent defects in a complex are nearest neighbors to each other. $\mu_e^{\rm int}$ is the Fermi-level position determined by native point defects. The solid dots connecting two energy segments with different slopes mark the defect levels.

TABLE IV. Peak absorption energy $(E_{\rm abs})$, peak emission energy $(E_{\rm m})$, Franck-Condon shifts $(d_{\rm FC}^{\rm e,g})$, Stokes shift (ΔS) , and thermal energy $(E_{\rm therm})$ associated with the Eu-related band–defect and 5d–4f optical transitions; all in eV.

Lattice site	$E_{\rm abs}$	$d_{\mathrm{FC}}^{\mathrm{e}}$	$E_{\rm em}$	$d_{ m FC}^{ m g}$	ΔS	$E_{ m therm}$	$E_{\rm abs}$	$d_{\mathrm{FC}}^{\mathrm{e}}$	$E_{\rm em}$	$d_{\mathrm{FC}}^{\mathrm{g}}$	ΔS	$E_{ m therm}$
	HSE: $\operatorname{Eu}_{\operatorname{Sr}}^0 \rightleftharpoons \operatorname{Eu}_{\operatorname{Sr}}^+ + e^-$						HSE: $\operatorname{Eu}_{\operatorname{Sr}}^{0}(4f^{7}) \rightleftharpoons \operatorname{Eu}_{\operatorname{Sr}}^{0,*}(4f^{6}5d^{1})$					
Sr1	4.86	1.04	2.71	1.11	2.15	3.82	3.91	0.22	3.42	0.27	0.49	3.69
Sr2	4.71	0.98	2.70	1.02	2.00	3.72	3.69	0.28	3.05	0.36	0.64	3.41
	$HSE: Eu_{Sr}^+ \rightleftharpoons Eu_{Sr}^0 + h^+$						$DFT+U:^{a} Eu_{Sr}^{0} (4f^{7}) \rightleftharpoons Eu_{Sr}^{0,*} (4f^{6}5d^{1})$					
Sr1	3.80	1.11	1.65	1.04	2.15	2.69	4.23	0.32	3.52	0.39	0.61	3.91
Sr2	3.81	1.02	1.81	0.98	2.00	2.79	4.00	0.29	3.38	0.33	0.72	3.71

^aDFT+U calculations with a computational setup similar to that in Jia et al., Phys. Rev. B **96**, 125132 (2017); see text.